Research Article | Vol. 11, No. 5 / 1 May 2021 / Optical Materials Express 1353

Optical Materials EXPRESS

Internal examination of mid-infrared chalcogenide glass optical fiber preforms and fiber using near-infrared imaging [Invited]

JOEL J. NUNES,* RICHARD W. CRANE, DAVID MABWA, DAVID FURNISS, MARK FARRIES, TREVOR M. BENSON, AND ANGELA B. SEDDON

Mid-Infrared Photonics Group, George Green Institute for Electromagnetics Research, Faculty of Engineering, University of Nottingham, University Park, Nottingham NG7 2RD, UK
eexjn6@exmail.nottingham.ac.uk

Abstract: We report on the internal examination of mid-infrared chalcogenide glasses using near-infrared light to reveal light-scattering defects. The technique is demonstrated on imperfectly made chalcogenide glass rods and fiber. This simple, non-destructive technique enables assessment of the interior of glasses and convenient detection of regions containing defects hidden due to the glass opacity to visible light. This method will reveal the presence of unwanted light-scattering defects including nucleated crystals, dust, striae, and bubbles. Hence, this method will help to optimize both chalcogenide glass chemical formulations, against devitrification, and process design to manufacture glass rods and fiber with minimized light scattering defects.

1. Introduction

Chalcogenide glasses are vitreous materials based on the chalcogen elements of Group XVI of the Periodic Table: sulfur 'S', selenium 'Se', and tellurium 'Te' [1]. Other p-block elements, such as: germanium 'Ge', arsenic 'As' and antimony 'Sb' are mixed with these chalcogens to form stable glass network structures. The heavier atoms and weaker covalent chemical bonding mean that the intrinsic phonon energy of the chalcogenide glasses can be lower than any oxide or fluoride glass giving the widest MIR (mid-infrared) window of all stable glasses to date. Currently, the useful, optical loss MIR transmission window of stable chalcogenide glasses in fiber form extends to 11 μm in wavelength [2]. The innate optical nonlinearity, based on greater polarizability of the chalcogens compared to oxides or fluorides, has led to their development as chalcogenide glass MIR supercontinuum (SC) broadband fiber lasers [3] and recent MIR-SC fiber device commercialization [4]. Lanthanide ion doping of chalcogenide glasses, usually with a gallium 'Ga', or indium 'In' co-solubilizer, has provided: new, bright MIR PL (photoluminescent) fiber sources [5], enabled new MIR fiber optical sensing based on PL molecular absorption of analytes [6,7], and MIR gain in chalcogenide glass fiber [8] and MIR lasing in bulk chalcogenide glass rod [9]; both gain and lasing are around 5 μm wavelength.

Manufacture of chalcogenide bulk glass and fiber requires several complex steps *viz.:* purification of chemical (usually elemental) precursors which includes their distillation, or fractional distillation driving off volatile impurities, followed by glass-batching and melting. Glass melting comprises heating precursors to above their liquidus, mixing, fining, and refining, then quenching and annealing. The glass may be further distilled followed by further quenching and annealing. Glass fibers may be made by reheating manufactured chalcogenide glass cullet using the double crucible technique [10,11] to draw down fiber, on a tower, under axial tension to achieve the desired fiber diameter. Alternatively, a chalcogenide glass cast rod or extruded billet may

#415518 https://doi.org/10.1364/OME.415518
Journal © 2021 Received 19 Nov 2020; revised 13 Jan 2021; accepted 14 Jan 2021; published 6 Apr 2021

Optical Materials EXPRESS

be drawn to unstructured fibre by reheating on a fiber tower, or stacked glass billets may be co-extruded and the extrudate similarly drawn to SIF (step index fiber) [12–14].

Returning to glass melting: this always culminates in rapid cooling of a true melt liquid from above the liquidus, through the liquidus to the supercooled liquid state. The supercooled liquid becomes increasingly viscous on cooling and forms a glass in the T_g (glass transition temperature) region. We name this the 'Melt-Quench' method. The Melt-Quench is followed by annealing at, or just above, T_g [15] which is an isothermal heat treatment (to maintain a constant fictive temperature across the glass to avoid leaving permanent stress) followed by slow-cooling to ambient (to maintain an isothermal temperature as far as possible during cooling to avoid thermal contraction mismatch and thermal shocking). Quenching, that is rapid cooling through the supercooled liquid region from the liquidus to T_g, is designed to avoid both heterogeneously and homogeneously nucleated crystallization, which is always free energy driven, as the supercooled liquid is metastable with respect to the crystal phase(s), and yet can be kinetically limited by limiting time spent in quenching. During the Melt-Quench method, bubbles may become entrapped in the final glass. Bubbles may be due to dissolved atmosphere liberated from the melt, or trapped vapor that was in equilibrium with the melt, or vacuum bubbles may arise, or a combination of these. A vacuum bubble can occur during quenching of the supercooled liquid if the outside surface of the article cools rapidly and sets solid at T_g, whilst the interior, still cooling as a supercooled liquid, is trying to contract as a liquid but restrained from doing so by the glass 'outer set-skin'. Then stress relief may occur by the interior melt pulling apart to leave a vacuum bubble; such a phenomenon has been observed on cooling fluoride glass rods of high aspect ratio (*Seddon and Furniss, unpublished work*). On first heating a chalcogenide batch during melting, the most volatile batch component is the S or Se chalcogen component. However, after some time for chemical combination at the melting temperature, then the vapor in dynamic thermal equilibrium above the melt is likely to be unimolecular species such as $GeSe_4$ or AsS_3 and so on.

Bubbles, crystals, and other unwanted defects are usually hidden from scrutiny due to the opacity of chalcogenide glasses, apart from pure sulfide glasses, to visible light. Here, we report on imaging such internal defects in chalcogenide glasses using a low cost, NIR (near-infrared) light source and NIR camera. We investigated non-destructively the interior quality of a chalcogenide glass rod preform, a rod boule and fiber, imperfectly manufactured, for instance due to non-ideal temperature control during the Melt-Quench method. These samples were illuminated with the NIR source and imaged orthogonally using a NIR camera to detect scattered light. Additionally, chalcogenide glass fibers were also illuminated and imaged using a NIR camera by transmission of NIR light along the sample. Chalcogenide glasses exhibit high refractive indices and the round section preform rods and fiber magnified internal defects during the NIR imaging. Therefore, to accurately measure dimensions of defects found whilst NIR imaging, a rod preform sample of chalcogenide glass was destructively evaluated using SEM-EDX (scanning electron microscopy with energy dispersive X-ray spectroscopy).

Section 2 describes the experimental methods of glass making, together with the non-destructive and destructive evaluation analysis. In Section 3 the results are presented, and they are discussed in Section 4.

2. Experimental

2.1. Preparation of bulk chalcogenide glass rod preform, rod boule and fiber by the Melt-Quench technique

Here we describe the Melt-Quench preparation of a particular chalcogenide glass rod preform further evaluated in Section 3. The glass rod preform was of nominal composition: $Ge_{19.4}$ $Sb_{9.7}$ $Ga_{3.0}$ $Se_{67.9}$ (*atomic %* (at%) ; (*code: M239RERC*)); mass: 29.574 g and dimensions: 10 mm cross-sectional diameter, 95 mm long and prepared from elemental precursors. Before batching, in order to remove volatile oxide impurities, Sb (*Materion: 5N*) was baked at 570 °C / 3 hours,

Optical Materials EXPRESS

and Se (*Materion: 5N*) at 260 °C / 2 hours, both under 10^{-3} Pa. Elemental precursors: Sb, Se, Ge (*Materion: 5N*) and Ga (*Alfa Aesar: 7N5*) were then batched (inside a *MBraun glovebox: N_2: < 0.1 ppm H_2O and < 0.1 ppm O_2*) into a low hydroxyl silica glass ampoule (*Multilab*: < 5 ppm OH) of inner / outer diameter: 10 mm / 14 mm (*prior air-baked, then vacuum-baked, both at 1000 °C /6 h*) and the ampoule was then vacuum-sealed at 10^{-3} Pa. The Melt-Quench technique was executed, thus: the melt ampoule was heated at 900 °C / 12 hours in a rocking furnace for melt homogenization; quenching was multi-step, comprising: a static vertical hold at 700 °C / 2 hours in the melt furnace for refining (*flotation of less dense impurities e.g. oxides*) and fining (Stokes' Law bubble rise) followed by a two-stage subsequent quench: (i) ampoule removed from furnace and cooled vertically, statically in air then (ii) a N_2 gas jet played on the vertical ampoule exterior starting at the top (*at the chalcogenide glass contracting cone)* and moving downwards, to encourage contraction of chalcogenide glass away from the inner ampoule wall. However, it should be noted that this process was under development and non-optimized at that time. The resulting glass rod was immediately annealed *in situ*, inside the ampoule, employing an isothermal heat treatment: 232 °C / 30 minutes before cooling with the furnace to room temperature (~ - 30 °C / h).

A further glass rod boule was similarly made (*nominally: $Ge_{14.8}$ $As_{20.8}$ $Ga_{2.0}$ $Se_{60.4}$ $S_{2.0}$ at. % (code: M278RC)*) with dimensions ~26 mm diameter and ~45 mm long. This glass was made according to [2].

Two separate stepped index chalcogenide glass fibers were made (*core nominally $Ge_{14.8}$ $As_{20.8}$ $Ga_{2.0}$ $Se_{62.4}$ at. % and cladding nominally $Ge_{14.8}$ $As_{20.8}$ $Ga_{2.0}$ $Se_{61.4}$ S_1 (codes: F105REJN and F117REJN)*). The preforms for the core and the cladding glass were made according to [2]. The cladding was subsequently extruded into a tube of inner / outer diameter: ~1 mm / 10 mm similar to [2]. The core glass rod preform was drawn to an intermediate unstructured cane, of diameter ~900 µm. This intermediate cane was inserted into the extruded cladding tube and the assembly drawn down to a (SIF) step-index fiber.

2.2. Non-destructive visible and NIR (near-Infrared) imaging of chalcogenide glass rod preform, rod boule and fiber

Non-destructive visible / NIR (near-infrared) imaging was carried out on the fabricated chalcogenide glass rods as follows. Using the set-up in Fig. 1, glass rods were mounted vertically in a rotational/XZ-translational stage and under-lit by illumination from a 20 mW LED, emitting light of center wavelength 940 nm. The visible / NIR camera (*ZWO ASI120MM Mini*) was mounted horizontally, relative to the vertical axis of the mounted rods and fiber, on a travelling microscope, atop a XY-translational stage to detect light scattered from samples.

Visible / NIR (near-infrared) imaging of fiber samples employed an optical microscope (*Vickers Instruments, model M171484*) and was carried out using the equipment configuration in Fig. 2. A 940 nm LED was abutted to the end of a fiber to launch light into the fiber. the opposite end of the fiber was positioned beneath the objective lens, on the XYZ-translational stage of the microscope to be imaged in either the visible or NIR spectral regions. The fiber samples were imaged in either a 'Side-inspection' or an 'End-inspection' configuration (see Fig. 2).

This NIR inspection technique is amenable to a variety of test conditions. Here, the glass rod sample was inspected in situ in its melt-ampoule. Thus, the ends of the glass rod sample were not polished. For fiber samples under 'end-inspection', both ends were cleaved orthogonally to the fiber axis using a Thorlabs Vytran Fiber Cleaver; the fiber ends were not polished.

2.3. Destructive evaluation of a bubble inside the rod preform

The visible / NIR imaging, described in Section 2.2, revealed the presence of two bubbles inside the rod preform. Thus, to investigate further one of these internal bubbles, the chalcogenide glass rod preform of nominal composition: $Ge_{19.4}$ $Sb_{9.7}$ $Ga_{3.0}$ $Se_{67.9}$ at. % was removed from

Optical Materials EXPRESS

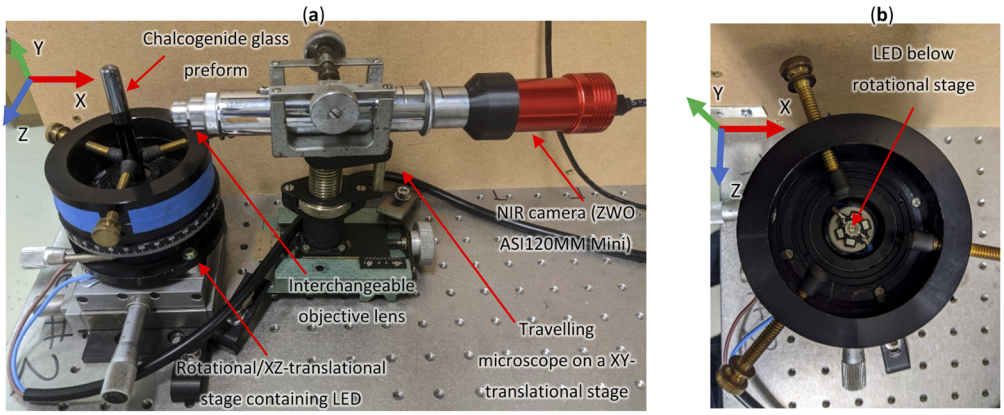

Fig. 1. Image of: (a) NIR imaging equipment configuration used to view inside chalcogenide glass rod preforms. Note that the XZ plane is the plane of the optical table. (b) Plan view of the rotational stage sample holder housing the stationary LED which illuminates the vertical rod from below (with chalcogenide sample removed).

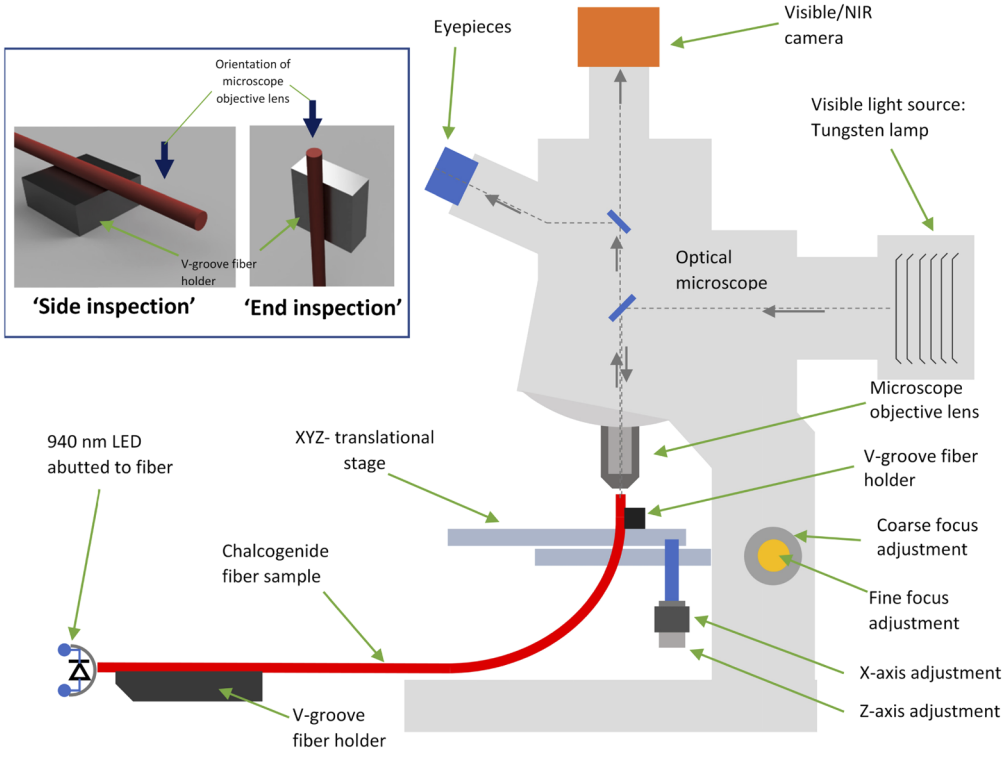

Fig. 2. Diagram of equipment configuration used to image chalcogenide fiber samples in either visible or NIR spectral regions. Showing a 940 nm LED abutted to the end of the chalcogenide fiber sample with the opposite end imaged by means of the optical microscope. Inset shows the orientation of the fiber sample and V-groove holder relative to microscope objective for 'Side inspection' and 'End inspection' on the microscope stage.

Optical Materials EXPRESS

its melt ampoule and scored with a diamond-coated blade circumferentially, close to a bubble defect and orthogonally to the rod long axis, which enabled a smooth orthogonal fracture to be actively guided by the presence of the bubble defect; the chalcogenide glass rod cracked open to reveal the hollow hemispherical cross-section of each half of the cleaved bubble. The size of the bubble defect was measured and then chemically analyzed using a JEOL 6490LV SEM- (scanning electron microscopy) fitted with an X-Max 80 Oxford Instruments EDX (Energy Dispersive X-ray spectroscopy) detector *(± 0.5 at. % accuracy for elements heavier than oxygen*).

3. Experimental results

3.1. Visible and NIR imaging

3.1.1. Chalcogenide glass rod preform both *in situ* in melt-ampoule and after removal

NIR imaging of the chalcogenide glass rod preform ($Ge_{19.4}$ $Sb_{9.7}$ $Ga_{3.0}$ $Se_{67.9}$ *at %*) *in situ*, in its silica glass melt-ampoule, shown in Fig. 3(a), revealed two prominent, (apparently) empty, spherical inclusions, namely: bubble 'A' and bubble 'B', originally hidden to the naked eye. Under NIR light, bubble 'B' was found to be located ~15 mm from the bottom of the 95 mm long (*~10 mm cross-sectional diameter*) rod and bubble 'A' was located about 15 mm above bubble 'B'. Figure 3(b) and (d) show the highly reflective nature of the bubble interfaces with the surrounding glass under NIR imaging.

On destructive analysis, and so cleaving open the chalcogenide glass rod preform (*see Section 2.3*), bubbles 'A' and 'B' were measured to be ~ 2 mm, and ~ 2.8 mm, in diameter, respectively (*see Fig. 3(c) and (e), respectively*). Bubble 'A' was asymmetrically positioned within the horizontal cross-section of the rod preform: about 4 mm in from the circumference of the 10 mm cross-sectional diameter preform. While bubble 'B' resembled a prolate spheroid and was approximately concentric within the horizontal cross-section of the rod preform. In summary, Fig. 3(b) to (e) together indicate the circular nature and the size of these bubbles. Bubble A was then imaged and chemically analyzed using SEM-EDX (*see Section 2.3*).

Adjacent to bubble 'B', NIR imaging also revealed the presence of what could have been suspended crystals in the glass (*see Fig. 3(f)*); polishing back to bring these to the glass surface would enable further inspection, analysis, and identification.

3.1.2. Chalcogenide glass rod boule

NIR imaging of the chalcogenide glass rod boule (*nominally* $Ge_{14.8}$ $As_{20.8}$ $Ga_{2.0}$ $Se_{60.4}$ $S_{2.0}$ *at. %*), of dimensions ~26 mm outside diameter and ~45 mm long, revealed no defects other than an unwanted filament within the preform (see Fig. 4). This filament had been originally hidden under visible illumination, and yet would have caused light scattering in any chalcogenide glass fiber ultimately drawn from this glass melt and acted as a potential fiber fracture site. This rod boule was not destructively analyzed, and the magnification imposed by the rod preform made it difficult to estimate the true size of this filament defect. However, to survive Melt-Quench processing (*see Section 2.1*) of the chalcogenide glass rod preform this filament must have been refractory and was probably ceramic in origin. We suggest its origin was a filament from refractory fibrous aluminosilicate blanket used in our lab to insulate the melt ampoule in the melting furnace. Filaments are about 10 microns in diameter and the mechanism for inclusion in the chalcogenide glass melt might have been atmosphere-borne either directly into the batching glovebox *via* a port or *via* the empty silica glass ampoule prior to batching. Optical microscopy showed that fibers from the aluminosilicate blanket had a diameter and length of 10 ± 2 µm and length 0.15 -3 mm, respectively.

Optical Materials EXPRESS

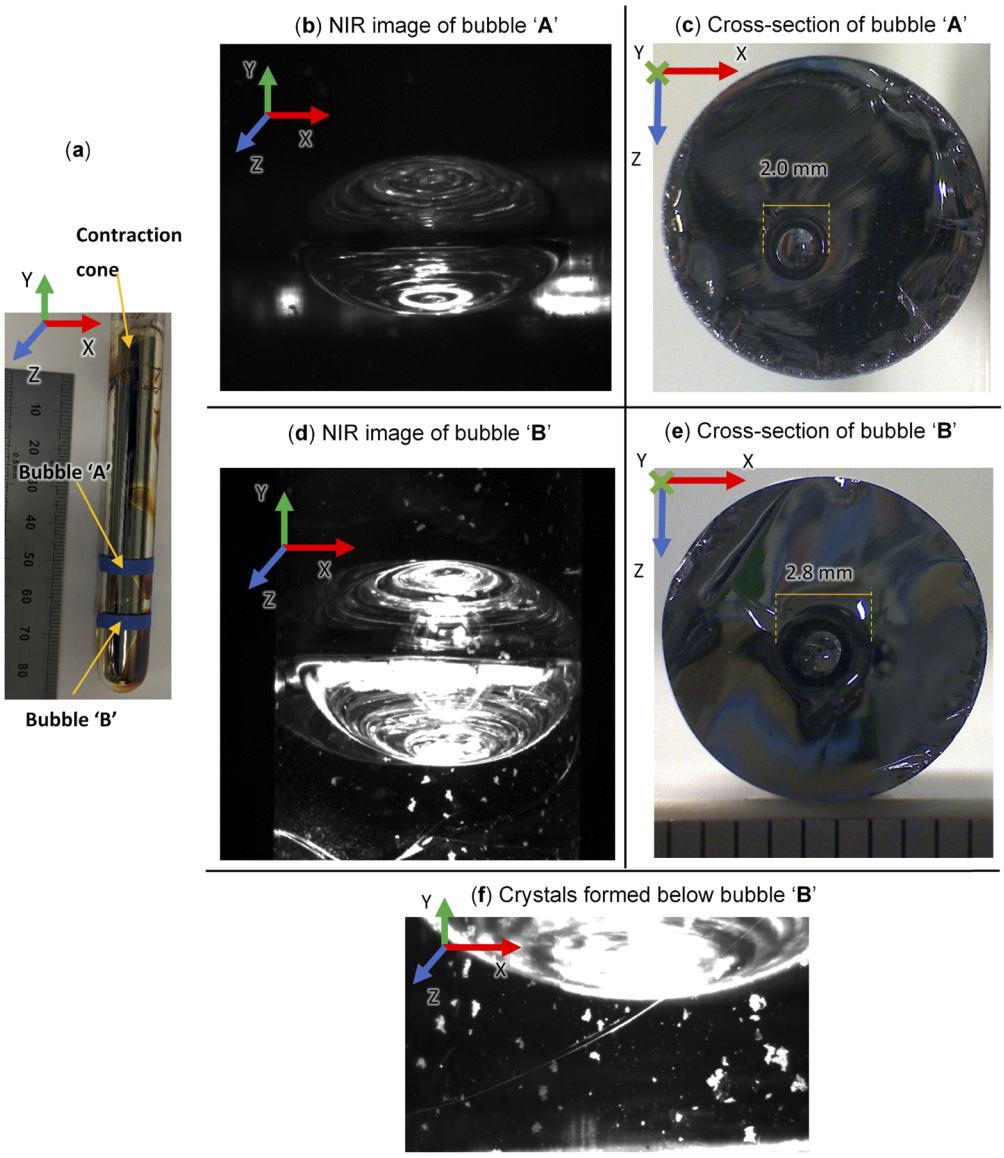

Fig. 3. Visible and NIR (near-infrared) imaging of chalcogenide glass rod preform (nominal composition: $Ge_{19.4}$ $Ga_{3.0}$ $Sb_{9.7}$ $Se_{67.9}$ at %). (**a**) Visible image (photograph) of glass preform with positions of bubbles marked using blue tape on surface of silica ampoule. (**b**) NIR image of bubble 'A', approximately 2.0 mm in diameter (shown in (**c**)). (c) Visible image of freshly cleaved preform showing a hollow hemispherical cross-section of bubble 'A'. (**d**) NIR image of bubble 'B', approximately 2.8 mm in diameter (shown in (**e**)). (**e**) Visible image of freshly cleaved preform showing hollow hemispherical cross-section of bubble 'B'. (**f**) NIR image of chalcogenide glass rod showing what may have been crystals formed in the vicinity below bubble 'B'.

Optical Materials EXPRESS

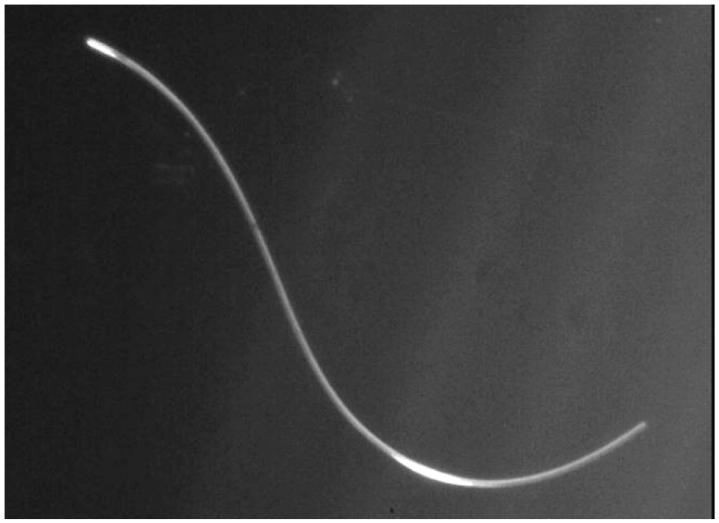

Fig. 4. NIR image of a chalcogenide glass rod boule (nominally $Ge_{14.8}$ $As_{20.8}$ $Ga_{2.0}$ $Se_{60.4}$ $S_{2.0}$ at. % dimensions ~26 mm diameter and ~45 mm long) revealing the unwanted presence of a filament suspended in the glass and thought to be refractory aluminosilicate from insulating blanket used in lab.

3.1.3. Chalcogenide step index fiber (SIF)

Two chalcogenide SIFs were investigated using visible and NIR imaging. Imaging the first SIF (*core nominally* $Ge_{14.8}$ $As_{20.8}$ $Ga_{2.0}$ $Se_{62.4}$ *at. % and cladding nominally* $Ge_{14.8}$ $As_{20.8}$ $Ga_{2.0}$ $Se_{61.4}$ $S_{1.0}$) of dimensions ~450 mm long, ~170 µm outside diameter, with a ~15 µm diameter core, revealed the core/cladding interface and two separate regions of unwanted refractive index striae (*i.e. small streaks of glass of different composition captured in the main glass*) in the cladding, originally hidden under visible illumination (*compare Fig. 5(a) and (b)*). The compositions

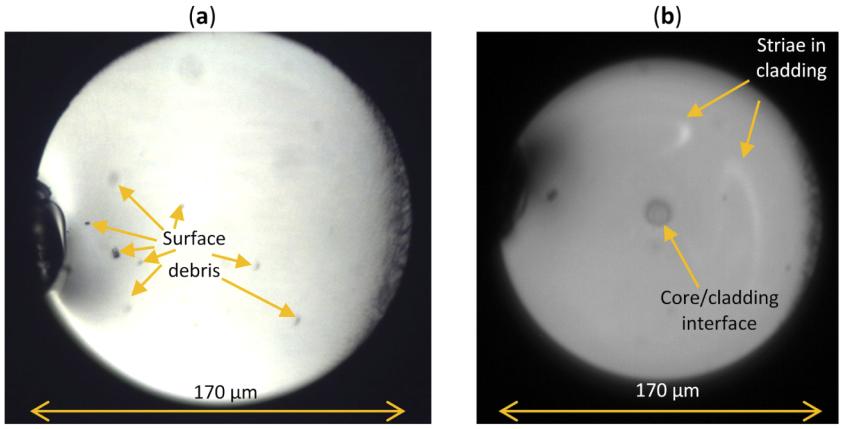

Fig. 5. Images of chalcogenide glass SIF (core nominally $Ge_{14.8}$ $As_{20.8}$ $Ga_{2.0}$ $Se_{62.4}$ at. % and cladding nominally $Ge_{14.8}$ $As_{20.8}$ $Ga_{2.0}$ $Se_{61.4}$ $S_{1.0}$) using 'End inspection' configuration with dimensions ~170 µm diameter with a ~15 µm core and ~450 mm long, (a) Image of cleaved fiber, utilizing visible illumination, showing extraneous surface debris and (b) NIR image of cleaved fiber showing core / cladding interface and striae in cladding.

Optical Materials EXPRESS

of the core and the cladding, as batched, nominally differed by 1 at. % sulfur, resulting in an indiscernible core/cladding interface under visible inspection (Fig. 5(a)). The inhomogeneity which caused the refractive index striae would most likely have been introduced prior to fiber drawing, during either the synthesis of the cladding glass rod boule or its subsequent extrusion. It is important to note that striae were observed only in glass tubes made by extrusion through a 'spider die'. The glass-melt splits as it passes through the die and recombines on exiting the die. The recombination could only produce striae for material with a pre-existing composition gradient. In ongoing work, we are carrying out in situ NIR imaging of the glass melt quenching process to explore not only bubble formation in the glass-melt, but also axial compositional homogeneity, potentially caused by high temperature volatilization and the effect of passing glass melts through extrusion dies.

Visible and NIR imaging of the second chalcogenide glass SIF of dimensions ~135 mm long, ~400 µm outside diameter, and ~37 µm diameter core, revealed an unwanted gap between the core and cladding. This may be seen in Fig. 6, under 'Side inspection' (*see Section 2.2*). It is known that this defect was due to lack of sufficient atmosphere control during rod-in-tube drawing.

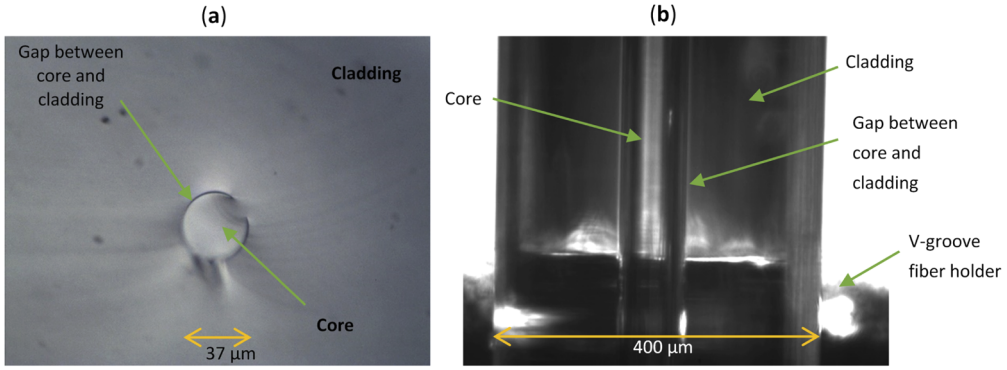

Fig. 6. Images of chalcogenide glass SIF (core nominally $Ge_{14.8}$ $As_{20.8}$ $Ga_{2.0}$ $Se_{62.4}$ at. % and cladding nominally $Ge_{14.8}$ $As_{20.8}$ Ga_2 $Se_{61.4}$ $S_{1.0}$) with dimensions ~400 µm outside diameter, ~37 µm diameter core and 135 mm long using: (**a**) 'End inspection' configuration with visible illumination showing gap between core and cladding, and (**b**) 'Side inspection' configuration utilizing NIR illumination again showing the gap between core and cladding.

3.2. SEM imaging and analysis of chalcogenide glass rod preform

SEM imaging and analysis of the chalcogenide glass rod preform ($Ge_{19.4}$ $Sb_{9.7}$ $Ga_{3.0}$ $Se_{67.9}$ *at.* %) was carried out to investigate the nature of bubble 'A' as shown in Fig. 3(a), (b) and (c).

Figure 7(a) and (b) show SEM images and compositional analysis using SEM-EDX of the freshly fractured glass surface and features on the inner wall of the bubble, taken from the general locations labelled as 'Area 1' and 'Area 2' in Fig. 7(a), respectively. SEM-EDX compositional analysis was carried out in Area 1 (SEM-EDX Scan #1) and in Area 2 (SEM-EDX Scans #2 and #3).

The composition determined at Scan#2 in Area 2, which lay just outside the perimeter of bubble 'A' and inside the host glass matrix. Scan#2 in Area 2 was determined to be: $Ge_{19.9}$ $Sb_{9.4}$ $Ga_{3.2}$ $Se_{67.5}$ at. %, which closely reflected the nominal composition of the as-batched glass: $Ge_{19.4}$ $Sb_{9.7}$ $Ga_{3.0}$ $Se_{67.9}$ at. %, as expected.

The composition determined at Scan#3 in Area 2, in contrast to Scan#2 in Area 2, lay inside the perimeter of bubble 'A' and, not only that, it appeared to have some debris accumulated at that site. Scan#2 in Area 2 gave the composition $Ge_{20.0}$ $Sb_{2.5}$ $Ga_{3.8}$ $Se_{73.7}$ at. % which was close

Optical Materials EXPRESS

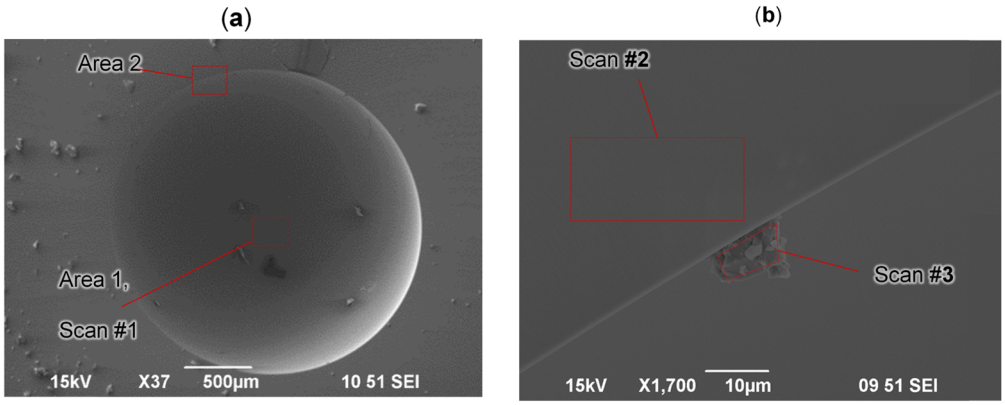

Fig. 7. Destructive analysis of chalcogenide glass rod preform (nominal composition: $Ge_{19.4}$ $Sb_{9.7}$ Ga_3 $Se_{67.9}$ at%). (a) SEM image of hollow cross-section of bubble 'A' (top of bubble 'A' relative to the position in the ampoule, see Fig. 3(a), (b) and (c)) SEM-EDX analysis is indicated as Areas 1 and 2; SEM-EDX analysis Scan #1 in Area 1 is also indicated. (b) Enlargement of Area 2 (from (a)) showing locations of SEM-EDX analytical scans #2 and #3 SEM-EDX analysis was: Scan #1 $Ge_{31.8}$ $Sb_{12.1}$ $Ga_{5.0}$ $Se_{51.1}$ at. %; Scan #2: $Ge_{19.9}$ $Sb_{9.4}$ $Ga_{3.2}$ $Se_{67.5}$ at. % and Scan #3: $Ge_{20.0}$ $Sb_{2.5}$ $Ga_{3.8}$ $Se_{73.7}$ at. %.

to the nominal composition of as-batched glass: $Ge_{19.4}$ $Sb_{9.7}$ $Ga_{3.0}$ $Se_{67.9}$ at. % except that the Sb content had decreased from 9.7 at. % to 2.5 at. %. We believe that the debris observed at this site was due to the glass fracturing process. But the low Sb content may indicate a change in chemical composition had occurred at the inside surface of the bubble.

Scan#1 in Area 1, in contrast to Scans#2 and #3 in Area 2, lay on the bubble surface deep inside the bubble 'A' relative to the cleave in a dip 1 mm deep (given that bubble 'A' was ~ 2 mm diameter). Scan#1 in Area 1 gave composition: $Ge_{31.8}$ $Sb_{12.1}$ $Ga_{5.0}$ $Se_{51.1}$ at. % which was significantly selenium deficient.

4. Discussion

The equipment configuration used here is amenable to different transparency windows of any glass or other materials, with choice of camera sensitive at the illumination wavelength. The low-cost of NIR hardware, coupled with the sensitivity and resolution of NIR cameras, makes this type of evaluation readily accessible as a rapid and convenient, non-destructive method of screening MIR-transparent chalcogenide glass preforms for bubbles, guiding usefulness for fiber-drawing and fiber quality after drawing and acting as a quality control on manufacture.

The glass rod preform (*see Section 3.1.1*), glass rod boule (*see Section 3.1.2*) and SIFs (*see Section 3.1.3*) were opaque in the visible spectral region, effectively hiding any internal defects. However, these chalcogenide glasses were moderately transparent at ~ 940 nm wavelength [16], enabling non-destructive imaging with the aid of the NIR 940 nm LED and visible/NIR camera.

The use of a bright NIR (940 nm) LED and NIR camera provided a low-cost solution for imaging inside the chalcogenide glasses, notwithstanding the relatively poor NIR transparency of the selenide glass samples [16]. Moreover, the rapidly changing NIR refractive index dispersion of the chalcogenide selenide glasses provided the advantage of optical contrast for > 1 at. % change in glass composition (see Fig. 5). In the MIR transparent window of the chalcogenide selenide glasses, glass optical loss is lowered but the imaging hardware is more costly.

Non-destructive IR imaging found two bubbles located inside the glass rod preform and destructive analysis, taking apart the glass rod preform, revealed their close proximity, and

Optical Materials EXPRESS

2-3 mm diameter, lying at a significant distance below the contraction cone (*see Fig. 3(a)*). SEM-EDX results showed the as-batched glass matrix was present outside the bubble 'A' perimeter (*see Fig. 7(b)*). Figure 7 shows a 16.4 atomic % deficit of Se, measured in the Scan #1 region (*interior surface of the bubble:* $Ge_{31.8}$ $Sb_{12.1}$ $Ga_{5.0}$ $Se_{51.1}$ *at. %*) compared to in the Scan #2 region (*bulk glass adjacent to bubble:* $Ge_{19.9}$ $Sb_{9.4}$ $Ga_{3.2}$ $Se_{67.5}$ *at. %*). It is proposed that during, and just after, bubble formation the bubble-interior surface-composition loses Se vapor to the bubble interior volume, possibly compounded with antimony, rendering the inner bubble surface both Se and Sb deficient (and increasing pro rata at. % of remaining elemental constituents). Furthermore, Fig. 7 shows a 22.6 at. % surplus of Se, measured in the Scan #3 region (*material located on the interior surface of the bubble:* $Ge_{20.0}$ $Sb_{2.5}$ $Ga_{3.8}$ $Se_{73.7}$ *at. %*) compared with the Scan #2 region. To account for this, it is proposed that Se-rich vapor released into the bubble volume from the bubble interior-surface will, as the system cools down, condense on the inner wall of the bubble. We note, however that additional investigation is required to properly confirm this hypothesis, and this forms our ongoing work.

The mechanism for bubble formation is suggested to be due to lack of control during the Melt Quench such that the outside of the rod preform quenched to below T_g and set as a solid glass skin, but the temperature of the inside of the rod preform was still rather too high and it was still contracting as a liquid yet prevented from doing so by the set-skin. In such cases, to relieve the thermal strain generated by this kind of mismatch in thermal contraction, vacuum bubbles may form. Initially any vacuum bubbles observed here may have been filled with a low-pressure vapor derived from the surrounding molten material. The discrepancy in composition between the inside of bubble 'A' and the glass outside found by SEM-EDX (*see Fig. 7 and caption*) lends credence to this suggestion.

Bubbles formed due to stress relief during melt quenching could fill with vapor in equilibrium with the surrounding glass melt, like $GeSe_4$ and would have condensed on the inside of the bubble during cooling to ambient. If instead the bubble contained species gaseous at ambient temperature, the gas laws would be obeyed giving lower pressure at ambient.

Vacuum bubbles are known to collapse during reheating for instance on fiber drawing. However, such collapse is likely not to be without penalty as the coming together of the bubble surfaces will likely leave a residual light scattering defect simply because the glass composition at surfaces would tend to be different from the bulk, having higher chemical potential.

The structural integrity and diameter stability of fibers drawn from a bubble-containing preform would be impaired, especially during the fiber drawing process itself. Due to the size of bubbles, these represent a significant change in volume and density of glass being heated up to fiber drawing temperature. It is also true that the local fiber diameter control may be affected as the local thermal inertia, heat capacity and thermal diffusivity during fiber drawing will all be affected by the presence of bubbles.

The NIR imaging of refractory filament (*see Section 3.1.2*) shows the capability for pinpointing unwanted sources of extrinsic light scattering in preforms and fiber. Here the large refractive index disparity between glass and inside of the bubbles led to bright light scattering. Similarly, capturing evidence of bulk crystallization (*see Section 3.1.1*) is excellent feedback to help optimization of glass formulations for eradicating devitrification and improving glass stability. Like all defects, it will be necessary to physically investigate the size and identity of crystals. Round section preforms with an optical flat introduced along the length would give instant feedback of defect size to overcome the lensing effect of round-section preform rods. This non-destructive evaluation method will be invaluable to reveal in MIR-transmitting chalcogenide glasses the presence of unwanted light-scattering defects including: homogeneously and heterogeneously nucleated crystals; intrinsic defects such as refractive index striae; extrinsic defects such as dust; and either gas-entrapped or vacuum bubbles, and imperfections at core-cladding glass interfaces of fiber preforms and optical fiber, and may provide insight into any surface-located defects. Hence, this

Optical Materials EXPRESS

method of preform and fiber evaluation will help to optimize both chalcogenide glass chemical formulations, against devitrification, and process design in order to manufacture chalcogenide glass optical fiber preforms and fiber with minimized light scattering defects in the finished fiber.

5. Conclusions

A non-destructive evaluation technique was used to appraise chalcogenide glass rod preforms and fiber samples which were opaque in the visible spectral region using near-infrared (NIR) imaging. Using this technique, the presence of unwanted light-scattering defects including: homogeneously and heterogeneously nucleated crystals; intrinsic defects such as refractive index striae; extrinsic defects such as dust; and bubbles, and imperfections at core-cladding glass interfaces may be detected. This technique allows for the convenient detection of regions containing hidden defects in a preform that is otherwise opaque to visible light. Thus, this evaluation method will help to minimize light scattering defects in finished glass rod preforms and fiber by aiding optimization of glass chemical formulations, against devitrification, and improving process design and manufacture of chalcogenide glass.

Funding. Engineering and Physical Sciences Research Council (EP/N50970X/1, EP/P013708/1).

Acknowledgements. The Authors are grateful for to the Nanoscale and Microscale Research Centre (NMRC) at the University of Nottingham, UK, for help and access to imaging and analytical electron microscopy.

Disclosures. The authors declare no conflicts of interest.

References

1. A. B. Seddon, "A review of their preparation, properties and applications," J. Non-Cryst. Solids **184**, 44–50 (1995).
2. D. Jayasuriya, C. R. Petersen, D. Furniss, C. Markos, Z. Tang, M. S. Habib, O. Bang, T. M. Benson, and A. B. Seddon, "Mid-IR supercontinuum generation in birefringent, low loss, ultra-high numerical aperture Ge-As-Se-Te chalcogenide step-index fiber," Opt. Mater. Express **9**(6), 2617–2629 (2019).
3. C. R. Petersen, U. Møller, I. Kubat, B. Zhou, S. Dupont, J. Ramsay, T. Benson, S. Sujecki, N. Abdel-Moneim, Z. Tang, D. Furniss, A. Seddon, and O. Bang, "Mid-infrared supercontinuum covering the 1.4–13.3 µm molecular fingerprint region using ultra-high NA chalcogenide step-index fibre," Nat. Photonics **8**(11), 830–834 (2014).
4. NORBLIS, "*Nordic Broadband Light Solutions*", (NORBLIS, 2020). https://norblis.com/
5. L. Sojka, Z. Tang, D. Jayasuriya, M. Shen, J. Nunes, D. Furniss, M. Farries, T. M. Benson, A. B. Seddon, and S. Sujecki, "Milliwatt-Level Spontaneous Emission Across the 3.5–8 µm Spectral Region from Pr^{3+} Doped Selenide Chalcogenide Fiber Pumped with a Laser Diode," Appl. Sci. **10**(2), 539 (2020).
6. F. Starecki, F. Charpentier, J.-L. Doualan, L. Quetel, K. Michel, R. Chahala, J. Troles, B. Bureau, A. Braud, P. Camy, V. Moizan, and V. Nazabal, "Mid-IR optical sensor for CO_2 detection based on fluorescence absorbance of Dy^{3+}:$Ga_5Ge_{20}Sb_{10}S_{65}$ fibers," Sens. Actuators, B **207**(Part A), 518–525 (2015).
7. A. B Seddon, "Mid-Infrared (MIR) Optical Sensing," in *Springer Handbook on Glass*, J. D. Musgraves, J. Hu, and L. Calvez eds., (Springer Handbooks, 2019).
8. M. Shen, D. Furniss, M. Farries, D. Jayasuriya, Z. Tang, L. Sojka, S. Sujecki, T. M. Benson, and A. B. Seddon, "Experimental observation of gain in a resonantly pumped Pr^{3+}-doped chalcogenide glass mid-infrared fibre amplifier notwithstanding the signal excited-state absorption," Sci. Rep. **9**(1), 11426 (2019).
9. M. F. Churbanov, B. I. Denker, B. I. Galagan, V. V. Koltashev, V. G. Plotnichenko, M. V. Sukhanov, S. E. Sverchkov, and A. P. Velmuzhov, "First demonstration of ~ 5 µm laser action in terbium-doped selenide glass," Appl. Phys. B **126**(7), 117 (2020).
10. IRflex, "*IRF-S Series Chalcogenide Mid-Wave Infrared (MWIR) Fiber (1.5 to 6.5 µm)*" (IRflex 2020) https://irflex.com/products/irf-s-series/
11. G. E. Snopatin, V. S. Shiryaev, V. G. Plotnichenko, E. M. Dianov, and M. F. Churbanov, "High-purity chalcogenide glasses for fiber optics," Inorg. Mater. **45**(13), 1439–1460 (2009).
12. K. Bhowmick, D. Furniss, H. P. Morvan, A. B. Seddon, and T. M. Benson, "Predictive, Miniature Co-Extrusion of Multilayered Glass Fiber-Optic Preforms," J. Am. Ceram. Soc. **99**(1), 106–114 (2016).
13. E. Roeder, "Extrusion of glass," J. Non-Cryst. Solids **5**(5), 377–388 (1971).
14. H. Ebendorff-Heidepriem and T. M. Monro, "Analysis of glass flow during extrusion of optical fiber preforms," Opt. Mater. Express **2**(3), 304–320 (2012).
15. D. Furniss and A. B. Seddon, "Thermal Analysis of Inorganic Compound Glasses and Glass-Ceramics," in *Principles and Applications of Thermal Analysis*, P. Gabbott, (Blackwell Publishing Ltd, 2008), Chap. 10.
16. L. Sojka, S. Sujecki, D. Furniss, Z. Tang, H. Sakr, A. B. Seddon, and T. M. Benson, "The Modelling of Fibre Lasers for Mid-Infrared Wavelengths," in *Recent Trends in Computational Photonics*, (Springer International Publishing 2017), Chap. 2.